

5-2013

# The effect of the local refractive index on the spectral properties of gold nanoparticle arrays

Justin Norman

*University of Arkansas, Fayetteville*

Follow this and additional works at: <http://scholarworks.uark.edu/cheguht>

---

## Recommended Citation

Norman, Justin, "The effect of the local refractive index on the spectral properties of gold nanoparticle arrays" (2013). *Chemical Engineering Undergraduate Honors Theses*. 6.  
<http://scholarworks.uark.edu/cheguht/6>

This Thesis is brought to you for free and open access by the Chemical Engineering at ScholarWorks@UARK. It has been accepted for inclusion in Chemical Engineering Undergraduate Honors Theses by an authorized administrator of ScholarWorks@UARK. For more information, please contact [scholar@uark.edu](mailto:scholar@uark.edu).

An Undergraduate Honors College Thesis

in the

\*\*\*\*\*

College of Engineering  
University of Arkansas  
Fayetteville, AR

by

This thesis is approved.

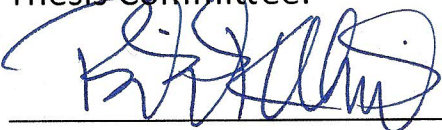
Thesis Advisor:



---

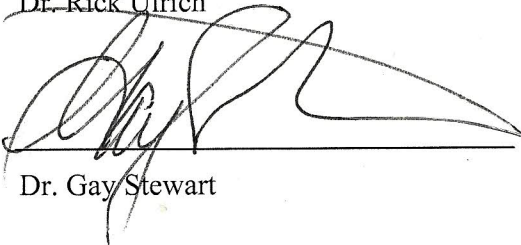
Dr. D. Keith Roper

Thesis Committee:



---

Dr. Rick Ulrich



---

Dr. Gay Stewart

## ACKNOWLEDGEMENTS

There have been many people involved without whom I would have never been able to complete this thesis. First, I would like to thank my research adviser, Dr. Keith Roper, who gave me the opportunity to work in his research group and supported every aspect of my work from applying for SURF grants to submitting my first peer-reviewed publication while also encouraging me in my work and life outside of the lab. He was involved in my project from the beginning to the end, and his insight in our private and group meetings proved invaluable. I feel that his guidance has greatly improved my research, technical writing, and communication skills and laid the groundwork for my future in scientific research. Dr. Gay Stewart, my physics adviser, provided guidance in choosing coursework to support my research interests and in producing a thesis appropriate for both of my majors.

I would also like to thank Drew DeJarnette and Dr. Phil Blake who were directly involved in my research. They taught me the fundamentals of scientific programming and provided critical insights throughout my research project. Their critiques of my writing also dramatically improved my ability to communicate my results in a clear and efficient manner.

I would also like to thank the Arkansas Department of Higher Education (ADHE) for awarding me a Statewide Undergraduate Research Fellowship for this project and the Walton Foundation whose Honors College Fellowship allowed me the freedom to take up undergraduate research.

Finally, I would like to thank my wife and parents for their encouragement and support.

# TABLE OF CONTENTS

<b>INTRODUCTION.....</b>	<b>3</b>
<b>THEORY.....</b>	<b>4</b>
<b>MODEL DEVELOPMENT.....</b>	<b>5</b>
<b>EFFECTS OF ARRAY/PARTICLE GEOMETRY ON SPECTRAL PROPERTIES.....</b>	<b>7</b>
<b>EFFECTS OF THE DIELECTRIC ENVIRONMENT ON SPECTRAL PROPERTIES.....</b>	<b>13</b>
<b>CONCLUSIONS.....</b>	<b>19</b>
<b>REFERENCES.....</b>	<b>20</b>

## Introduction

Understanding the interaction between electromagnetism and condensed matter has opened the door to major advances in the fields of medicine, computation, sustainable energy, and telecommunications. Techniques such as magnetic resonance imaging and X-ray scanning have allowed for previously unprecedented diagnostic capabilities. Constant improvements in the efficiency of photovoltaics could be paving the way to a future of clean, renewable energy. The ability to transmit optical signals over long distances and through fibers has revolutionized the way society operates by allowing for high-speed data transfer and wireless communication. Each of these developments has had a tremendous impact on society and is only a small fraction of what might one day be achieved. With the relatively recent discovery of the unique ways electromagnetic waves interact with matter at subwavelength scales, the door has been opened even wider to revolutionary new technologies.

Specifically, the burgeoning field of plasmonics has demonstrated capabilities previously unimaginable. In the past, the diffraction limit seemed to be an impassable barrier to imaging and waveguides, but now modern technology has moved far beyond the Rayleigh limit with successful image resolution at one-sixth of the incident wavelength<sup>1</sup> and production of waveguides that are limited only by the atomic structure of matter, dissipation, and the spatial dispersion of light<sup>2</sup> both of which take advantage of the unique properties of plasmonic materials. Meanwhile, the concept of an invisibility cloak, previously relegated to the realm of science fiction, has been experimentally realized at both microwave and visible wavelengths for sizes up to the centimeter scale using related technology.<sup>3,4</sup> Yet another development brought about by the study of plasmonics is the experimental detection of a single molecule in solution.<sup>5</sup> This ultimate level of sensing precision could have significant implications in medicine and pharmacology. The remarkable fact is that these are but a few of the incredible applications for plasmonic technologies that have already been developed. Others include further advances in medicine<sup>6,7,8</sup>, sustainable energy<sup>9,10</sup>, and informatics<sup>11</sup> to name but a few.

A unifying trend in each of the previously mentioned applications of plasmonic composites is that they were first theoretically hypothesized and subsequently observed experimentally. This historical precedent demonstrates the need for characterization of new, engineered materials and composites such that their unique properties can be fully described in the space of their specifications (composition, geometry, environment, etc.) and ideal applications can be identified and tested experimentally in the most efficient manner possible.

In this thesis, a relatively new type of composite consisting of planar spherical gold nanoparticle arrays<sup>12</sup> is thoroughly characterized in terms of the

particle size, spacing, array size, and the local dielectric environment<sup>13</sup>. Gold (and other metals capable of sustaining a plasmon resonance such as silver and copper) nanoparticle arrays respond to incident electromagnetic radiation in a manner of interest for many of the previously mentioned plasmonic technologies. Such arrays have been investigated theoretically<sup>14</sup> and experimentally<sup>15</sup> in previous work for specific geometries and compositions. This work was an important component of the ongoing parametric investigation of each of the contributing factors to an array's optical properties and the identification of the underpinning phenomena that result in the most ideal optical response in the Nano Bio Photonics Lab<sup>12,13,14,15</sup>. Gold was selected for this study because it is of particular interest in many applications due to its high resistance to oxidation.

## Theory

Incident electromagnetic radiation on subwavelength metallic nanoparticles results in collective oscillation of the conduction electrons of each nanoparticle in the direction of polarization. The amplitude of this oscillation is maximized for a particular frequency of the incident wave. This phenomenon is termed the localized surface plasmon resonance (LSPR). The collective oscillation of electrons effectively creates a dipole for small particles with higher order modes becoming prevalent for larger particle sizes. The specific range of wavelengths that corresponds to the LSPR is dependent on the material, particle size, and the local dielectric environment and is observed experimentally through the detection of a spectral absorption peak maximized at the LSPR wavelength. The spectral response of single particles is described analytically by Mie theory.<sup>17</sup>

When metallic nanoparticles are organized into arrays, the electromagnetic fields of neighboring particles couple resulting in enhancement of the LSPR with further enhancement due to constructive interference of radiation scattered from the individual particles in the plane of the array. This scattered radiation will constructively interfere at the site of individual particles for wavelengths equal to the particle spacing, termed the lattice constant,  $D$ , for axial coupling and  $D/\sqrt{2}$  for diagonal coupling, and so on for higher order modes, resulting in amplification of the electric field. The net result of these effects is that the optical extinction profile will exhibit a series of features corresponding to the LSPR, constructively interfering radiation scattered axially, diagonally, and along other modal directions in the array, all of which are coupled through the particle polarizability<sup>18</sup>.

Experimentally, the LSPR is represented by a broad band extinction peak while the peak from scattered radiation is a narrower Fano resonance. The diagonal peak is typically suppressed for reasonable lattice spacings because coupling between electromagnetic radiation and the LSPR is not supported for wavelengths

less than the LSPR wavelength<sup>19</sup>, which for gold is typically greater than 510 nm. The fundamental physical and geometrical parameters that characterize each of the aforementioned spectral features are explored in detail in the following sections with particular emphasis on the coupled peak due to its significant extinction magnitude and narrow linewidth that would be found desirable in many applications.

## Model Development

Theoretical characterization of arrayed plasmonically active particles is typically done numerically using techniques such as the finite difference time domain (FDTD) or T-matrix methods or through approximations such as the discrete dipole approximation (DDA) and coupled dipole approximation (CDA); however, these methods are computationally inefficient making them impractical for mapping out a broad parameter space describing the parametric effects of the array and particle geometry and dielectric characteristics on the array's spectral response. To combat these issues, a model was developed<sup>12,13,14</sup> that uses the CDA and takes advantage of symmetry in square arrays to dramatically enhance computation efficiency for the case of spherical particles.

The CDA treats each particle in the array as a point dipole which reduces the particle polarizability,  $\alpha$ , to an effective, scalar value. The polarizability can be calculated for spherical particles in terms of a multipole expansion of size-dependent effective multipole polarizabilities<sup>20</sup>, viz.

$$\alpha = \frac{3iR^3}{2x^3} a_1 + \frac{10iR^3}{3x^3} a_2 \quad (1)$$

where  $R$  is the particle radius,  $x = k\eta R$  is the size parameter with wavenumber  $k$  and medium refractive index  $\eta$ , and  $a_1$  and  $a_2$  are the complex Mie coefficients corresponding to the dipole and quadrupole modes respectively from Mie Theory<sup>17</sup> and described in Eq. (2). Higher order modes than quadrupole were found to not make significant contributions for particle radii up to 120 nm and were omitted from calculations<sup>18</sup>.

$$a_n = \frac{m\Psi_n(mx)\Psi'_n(x) - \Psi_n(x)\Psi'_n(mx)}{m\Psi_n(mx)\xi'_n(x) - \xi_n(x)\Psi'_n(mx)} \quad (2)$$

In Eq. (2),  $\Psi_n$  and  $\xi_n$  are the Riccati-Bessel functions and  $m = \varepsilon^{1/2}\eta_0^{-1}$  is the ratio of the dielectric constant of the metal to that of the environment. The particle polarizability can be used to calculate the extinction cross section,  $C_{\text{ext}}$ ,<sup>21</sup>



$$C_{ext} = \frac{4\pi k}{|\mathbf{E}_{inc}|^2} \sum_{j=1}^N \text{Im}\{\mathbf{E}_{inc,j}^* \cdot \mathbf{P}_j\} \quad (3)$$

where  $\mathbf{E}_{inc}$  is the incident electric field and  $\mathbf{P}_j$  is the polarization of particle  $j$ . Eq. (3) can be simplified by treating the array as infinite and applying the previously described polarizability term to get

$$C_{ext} = 4\pi k \text{Im} \left( \frac{\alpha}{1 - \alpha S} \right) \quad (4)$$

where  $S$  is the retarded dipole sum<sup>22</sup>. The actual numerical value of the extinction cross section is not directly relevant but should instead be considered in relating peaks in the extinction amplitude to each other. For the purposes of the analysis presented here, the extinction cross section is presented in arbitrary units.

The retarded dipole sum, defined in Eq. (5), is a parameter that accounts for the contributions of the scattered radiation from every particle in the array to the local electric field of the center particle.

$$S = \frac{e^{ikr_{ij}}}{4\pi\epsilon} \sum_{i \neq j} \frac{(1 - ikr_{ij})(3\cos^2\theta_{ij} - 1)}{r_{ij}^3} + \frac{k^2 \sin^2\theta_{ij}}{r_{ij}} \quad (5)$$

The retarded dipole sum is derived from solving for the polarization of one particle in terms of the electric field contribution from the incident radiation and the oscillating dipoles of neighboring particles<sup>22</sup>. The array is then approximated as being infinite, so each particle polarization can be treated identically yielding

$$\mathbf{P} = \alpha \mathbf{E}_{loc} = \frac{\mathbf{E}_{inc}}{\frac{1}{\alpha} - S} \quad (6)$$

where  $\mathbf{E}_{loc}$  is the local electric field at the center particle. By considering only square arrays and taking advantage of symmetry, the retarded dipole sum can be determined for the entire array from calculations for only one quadrant. The end result is that the CDA can be computed for a given array for a factor of eight fewer function calls than it would have taken to perform the full CDA considering each element independently. This new version of the CDA has been termed the rapid semianalytic CDA (rsa-CDA)<sup>12,13,14</sup>.

To assess the model's validity, the extinction cross section was calculated across the visible spectrum and compared with the results from Mie Theory for a single gold particle and FDTD for a large array of gold particles<sup>18</sup>. The results are shown in Figure 1. A virtually perfect fit was observed between the rsa-CDA and Mie Theory for particles smaller than 120 nm in radius with some divergence for larger particles due to the increasing dominance of higher order modes than quadrupole. Accounting for higher order modes by including additional terms in Eq. (1) is constrained by the increasing geometric complexity of these modes which precludes their treatment as dipole interactions.

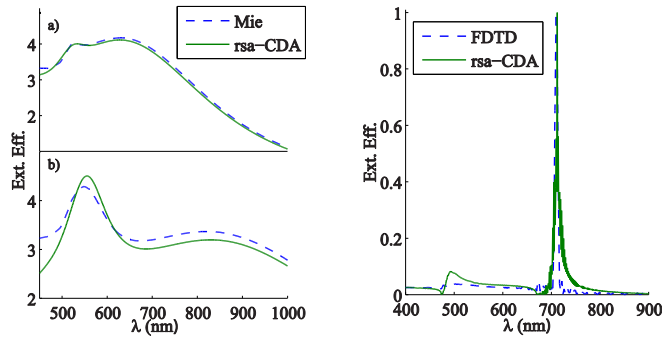


Figure 1. Reproduced from [18]. Extinction efficiency found using Mie Theory and the rsa-CDA for single gold particles with radii (a) 110 nm and (b) 150 nm. Also displayed is the extinction efficiency for an array of 110 nm gold particles with a spacing of 670 nm calculated using FDTD and the rsa-CDA.

Meanwhile, for an array of 110 nm gold particles, spaced 670 nm apart, there is strong agreement between the rsa-CDA and FDTD with two minor exceptions<sup>18</sup>. One exception is that the rsa-CDA gives two zeros in the extinction efficiency due to singularities in the retarded dipole sum for wavelengths on the order of the diagonal and axial particle separation. The second deviation is an exaggeration of the diagonal peak. By treating the quadrupole mode as a single dipole instead of a pair of oppositely oriented dipoles, the coupling of the scattered radiation is exaggerated. These deviations are not significant to applications because the coupled peak and diagonal peak are always of longer wavelength than, redshifted from, the particle spacing on their respective axis as will be described in the following sections.

## Effects of Array/Particle Geometry on Spectral Properties

The spectral properties of plasmonic nanoparticle arrays are driven by two coupled phenomena. One is the plasmon resonance of the individual particles whose effect is encapsulated in the individual particle polarizability. The second phenomenon is the scattering (reradiation) of light in the plane of the array. Depending on the phase of the scattered radiation relative to the plasmon resonance at a given particle, constructive or destructive interference from particles in the array

can occur resulting in either enhanced or suppressed optical extinction. Each of these phenomena is directly tied to the size, shape, composition, and arrangement of the arrayed nanoparticles.

For isolated particles, the wavelength of maximum optical extinction corresponds directly to the wavelength that maximizes the imaginary part of the dipole and/or quadrupole polarizability. This result is seen when comparing Figure 2, plots of the imaginary part of the particle polarizability for a range of wavelengths and particle radii, with the plots in Figure 1 (a) and (b). In addition to being an indicator of the wavelength of the extinction maxima, the polarizability is also proportional to the amplitude of the extinction peak. For instance, in going from Figure 1 (a) to Figure 1 (b) on the polarizability plot of Figure 2, an increase in the magnitude of the quadrupole peak can be observed relative to that of the dipole peak which cannot simply be a product of the chosen polarizability model because it is corroborated by the results from Mie Theory and FDTD also presented in Figure 1 (dashed lines).

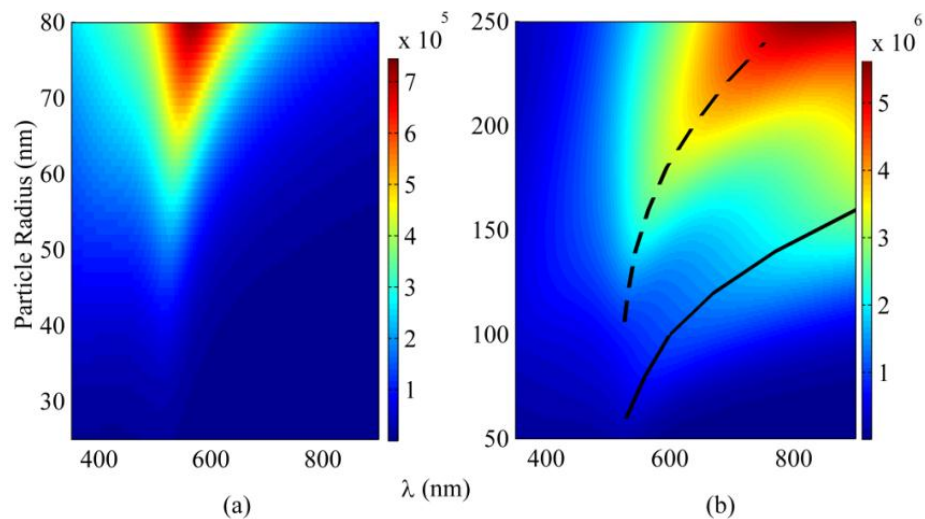


**Figure 2.** Reproduced from [18]. The imaginary part of the particle polarizability is plotted as a function of particle radius and incident wavelength for a single gold nanoparticle. In (b) the solid line represents maximum dipole polarizability while the dashed line corresponds to maximum quadrupole polarizability. The two plots overlap between 50 and 80 nm, but the color scale in (b) is an order of magnitude larger to adequately capture the trends.

In order to understand how these individual particle effects and scattered radiation in an array interact, it is useful to consider the radiative scattering patterns for the dipole and quadrupole resonance modes of individual particles. The scattering patterns for the dipole (a) and quadrupole (b) modes calculated using spherical harmonics are displayed in Figure 3<sup>18</sup> for nanoparticles arranged in the x-y plane subjected to incident radiation orthogonal to the plane and polarized in the x-

direction. The coloration represents the phase of the scattered radiation. Positive phase contributions are displayed in red, and negative contributions are in blue.

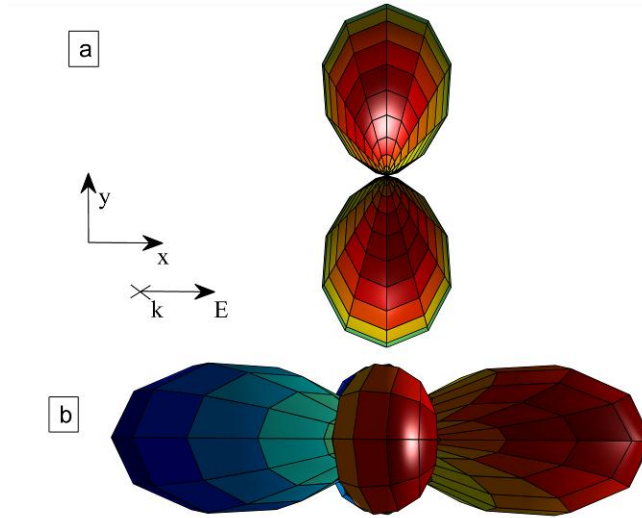


**Figure 3.** Reproduced from [18]. The planar scattering phase patterns for (a) dipole and (b) quadrupole LSPR modes of individual particles are displayed for incident polarization in the x-direction. The relative phase is distinguished by color with red being positive and blue negative.

From Figure 3, the dominant in-plane scattering directions can be clearly identified as the directions parallel and orthogonal to the incident polarization for the quadrupole and dipole modes respectively, but due to the difference in phase for scattered radiation from the quadrupole mode along the polarization axis (x-axis in Fig. 3), destructive interference significantly reduces coupling in that direction. This leaves the direction orthogonal to the polarization (y-axis) as the primary direction of coupling with relatively small contributions from particles situated between  $\theta = 0^\circ$  and  $90^\circ$  of the polarization direction relative to a given center particle because the scattering amplitude scales as  $\sin^2 \theta$ . For larger particle sizes with dominant quadrupole and higher order modes, the scattering patterns become more complicated but are not considered here because the rsa-CDA only considers smaller particles where the dipole mode dominates.

Since the unique features of nanoparticle arrays result from coupling between the LSPR and constructively interfering scattered radiation, one would expect there to be a coupling in the effects of changing particle size and lattice constant on the wavelength corresponding to the coupled peak. This coupling has been observed using the rsa-CDA<sup>18</sup> and other models<sup>11,22,23</sup>. The result is a redshift and broadening of the coupled peak away from a wavelength equivalent to the lattice constant, where constructive coupling would begin, with greater shifting at smaller lattice constants<sup>20</sup> and is displayed in Figure 4. An explanation of this phenomenon lies, yet again, in Figure 2 and, by association, the polarizability of the individual particles of the array. With decreasing lattice constant, and thus the wavelength resulting in

constructive interference, the polarizability increases for constant particle radii. Increased polarizability means weaker electric fields are necessary to obtain a given polarization meaning lower energy photons are capable of exciting the nanoparticle electrons to resonance thus broadening the extinction band toward longer wavelengths as seen in the inset of Figure 4.

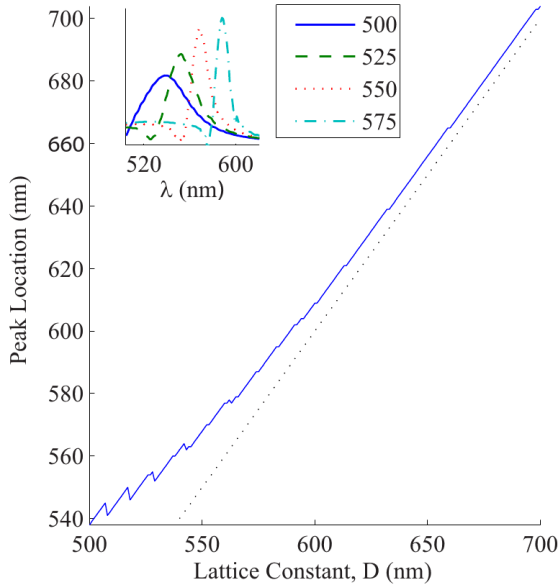


**Figure 4.** Reproduced from [18]. The location of maximum extinction (solid line) of the coupled peak is plotted as a function of the particle separation for an array of 65 nm gold particles. The dotted line represents a 1:1 correspondence between the lattice constant and peak location. The inset shows the coupled peak for a range of specific lattice constants.

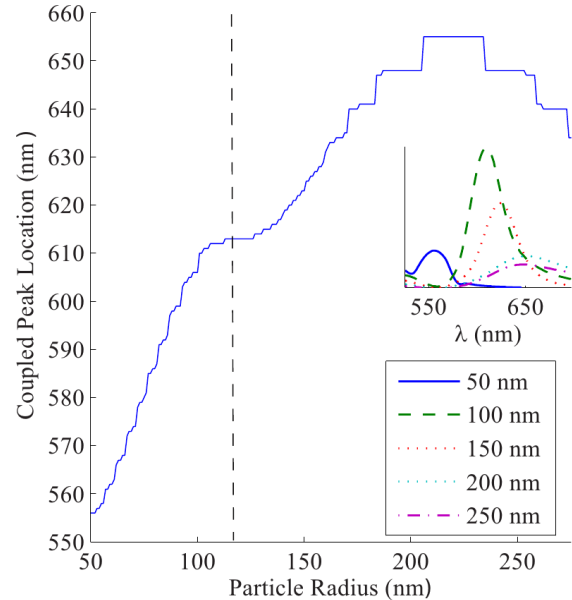


**Figure 5.** Reproduced from [18]. The coupled peak location for a lattice constant of 550 nm is plotted for various particle radii. The dashed line indicates the particle radius for which the contributions from the dipole and quadrupole LSPR modes are equivalent. The inset shows the coupled peak for a range of particle radii.

Similar logic can be used to explain the trends with increasing particle radius. As the particle radius increases for a constant lattice spacing, the polarizability increases leading to a lower energy barrier for resonance and redshifting and broadening of the coupled peak, but there is an added complication. With increasing particle radius, additional resonance modes appear leading to certain ranges of particle radius where the coupled peak wavelength is constant as shown in Figure 5 at radii between 110 nm and 140 nm and a wavelength of 615 nm. For this range of geometries the resonance mode is shifting from a predominantly dipole to quadrupole mode. During the transition, exactly opposing changes in the dipole and quadrupole resonance resulting in no net effect on the coupled peak. Continuing to larger particle radii, the roughly linear trend returns and then shifts to a step-like pattern reaching a maximum around 655 nm and then decreasing. In this region, the quadrupole mode begins to wane with higher order modes taking over, but due to the chosen polarizability model, higher order modes were not included.

Having characterized the coupled peak wavelength in terms of the geometric parameters of the array, the logical next step is to investigate how these same parameters affect the amplitude of the coupled peak. As was the case previously, the polarizability of an array's constituent particles continues to play a prominent role. A surface plot of the amplitude of the greatest extinction peak as a function of particle radius and lattice constant is presented in Figure 6. The amplitude of the extinction cross sections were truncated at 2000 to prevent certain geometries with particularly high extinctions from washing out the overall trends.

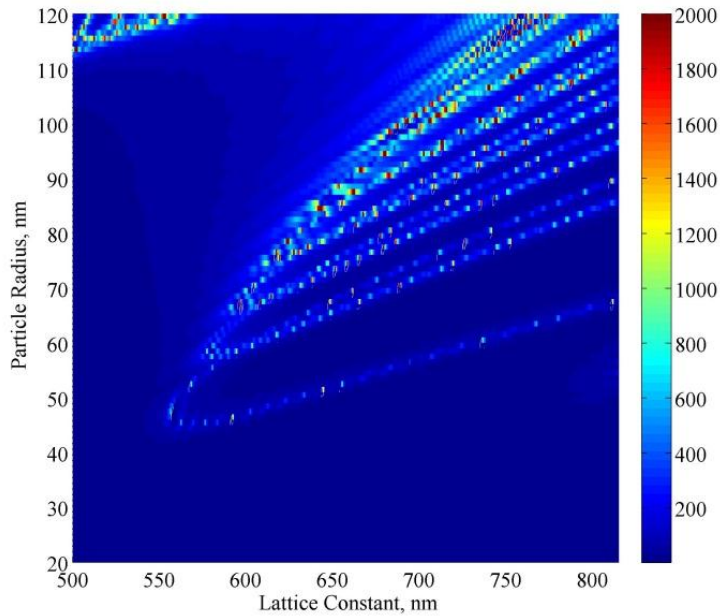


**Figure 6.** The amplitude of maximum extinction is plotted for a range of particle radii and lattice constants for an array of gold nanoparticles. Extinction values were truncated at 2000 to prevent smaller peaks from being washed out.

Several notable trends can be observed in Figure 6. First, there is no significant coupling for particle radii below 44 nm. This can be explained by the fact that absorption rather than scattering dominates in smaller particles. If light is not scattered in a sufficient amount, there will not be significant coupling in the array.

A second trend is that the geometries that give the maximum coupling seem to form a series of overlapping parabolas that are increasingly narrow and more frequent at higher particle radii. To examine the source of these parabolas, two points (array geometries) were taken from along the lowest line: (599, 50) and (696, 60). The individual spectra corresponding to these two geometries were investigated and the coupled peak wavelengths were found to be 599 nm and 696 nm respectively. Taking these wavelengths and returning to the polarizability plot of Figure 2 yields polarizabilities of  $0.5604 \times 10^5$  and  $0.5619 \times 10^5$  for the two configurations revealing that the regions of maximum extinction for the coupled peak correspond to isometric

values of the particle polarizability. This important result was first noted in [18]. They essentially follow specific contours of Figure 2.

The third trend, the increasing frequency of regions of high extinction as particle radius increases with an unchanging lattice constant, can be explained by breaking the array up into individual chains of particles and considering independently each of their contributions to the scattered radiation on a center particle. First, recall that as particle radius increases, so does the ratio of scattering to absorption. Next, consider Figure 7 where each distinct color of particle is equidistant from the center particle and contributes a distinct excitation mode of the form presented in Figure 3 (hence no coupling in the direction of polarization due to cancelations in the quadrupole phase and zero contributions from the dipole resonance).

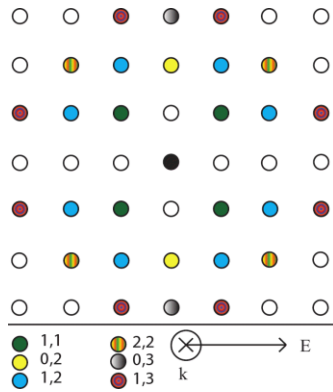


**Figure 7. Reproduced from [18].** A section of an array of particles is displayed with equidistant particles color coded to illustrate the unique scattered phase contributions of various particle chains within in array.

The various modes displayed can be divided into axial, diagonal, and off-axial-off-diagonal (OAD) contributions. From a geometrical perspective, it is clear that the axial contributions will be greatest followed by the diagonal contributions with the OAD chains giving the smallest contributions to the scattered radiation. The attenuation with distance of scattered radiation in the array causes the diagonal contributions to be less than the axial contributions due to the larger particle spacing along the diagonal. Meanwhile, the OAD particles are not only spaced even farther apart than the diagonal particles, but they are also fewer in number for a given chain meaning there are fewer sites for scattering to occur. The number of particles and particle separation in each chain determines the chain's individual contribution in phase to the center particle's; therefore, the phase of the axial particles will dominate with smaller contributions progressively from the diagonal and OAD chains, but for certain geometries the sum of the diagonal and OAD chains can destructively interfere with axial coupling resulting in suppression of the coupled peak.

## Effects of the Dielectric Environment on Spectral Properties

In different environments nanoparticle arrays with identical geometric specifications can have completely different optical extinction profiles. Two primary phenomena contribute to the changes in the extinction profile with changing environments. The first is wavelength compression. Relative to vacuum, electromagnetic waves compress when they travel through media by a factor of the refractive index (RI). The second phenomenon is that the surrounding dielectric will become polarized due to the electric fields of the incident radiation and plasmon resonance. This polarization enhances the plasmon oscillation by counteracting the restoring force from the positively charged core of a particle.

### Single Particles

As previously stated, wavelength compression is the driving force behind changes to the spectral properties of an array for different dielectric environments. Wavelength compression poses an obvious issue in array design because the peaks in the extinction spectra are dependent on the interference effects of the scattered radiation in the plane of the array. With changes in the homogenous background RI,  $\eta$ , the wavelength that yields constructive interference for a given lattice constant will change. Wavelength compression also results in the formation of higher order modes due to a decrease in the size of the wavelength relative to the particle radius as illustrated in Figure 8(a) and demonstrated for a single gold nanoparticle with a 70 nm radius in Figure 8(b). The formation of higher order modes is of significant concern because it reduces the maximum particle size that can be reliably modeled using only the dipole and quadrupole terms while also affecting which resonance modes will be dominant in particle coupling.

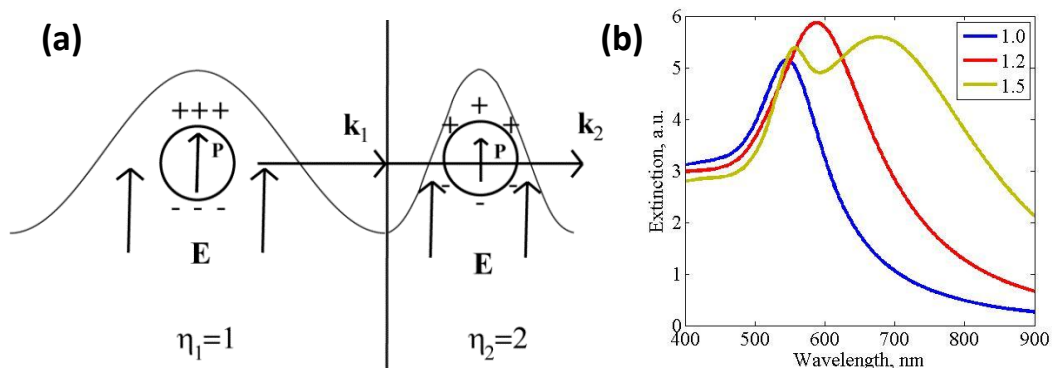
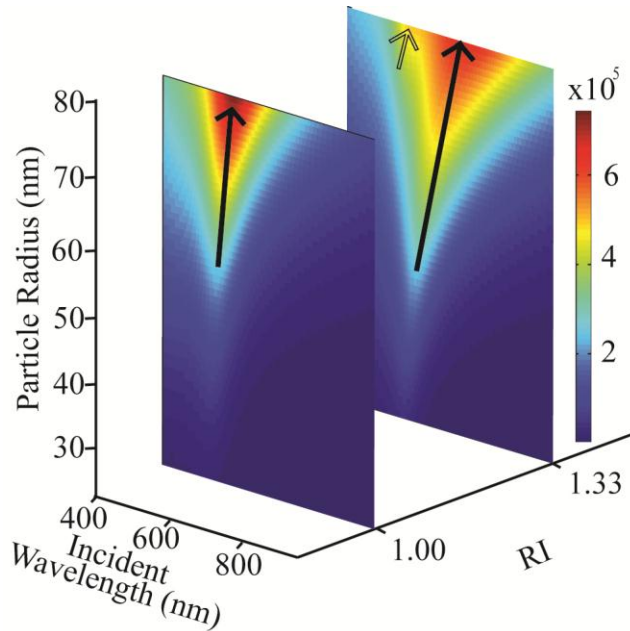


Figure 8. (a) depicts the effects of wavelength compression on nanoparticle polarization for a plane wave traveling from a region of lower refractive index to a region of higher refractive index. (b) The extinction profile of a 70 nm gold nanoparticle is displayed as a function of the vacuum wavelength for RIs of 1.0, 1.2, and 1.5 to illustrate the formation of higher order modes for increasing RI with constant particle radius.



Another observation that can be made from the results in Fig. 8(b) is that there is a broadening and redshifting of the plasmon peak with increasing refractive index. This is the result of an induced polarization in the dielectric medium that dampens the Coulombic restoring force of the positively charged core of the particle. By dampening the restoring force, a broader range of lower energy (longer wavelength) photons are capable of exciting the conduction electrons of the particle to resonance.



**Figure 9. Reproduced from [13]. The imaginary part of the individual particle polarizability is plotted as a function of particle radius and incident wavelength for RI values of 1.00 and 1.33. The black arrow represents the maximum values corresponding to the dipole mode, and the grey arrow represents the maximum values corresponding to the quadrupole mode.**

In Figure 9, the polarizability for a single gold particle is plotted as a function of the particle radius and incident wavelength for two values of the refractive index. As the refractive index increases from 1.00 to 1.33, the wavelength yielding the maximum values for polarizability redshifts, and the amplitude of the polarizability increases for smaller particles which relates back to the previously mentioned polarization of the dielectric medium. For larger particles, the overall amplitude decreases because the quadrupole mode increases in influence relative to the dipole mode as illustrated by the arrows in Fig. 9 with the black arrow representing the dipole mode and the grey arrow representing the quadrupole mode.

### Arrays

Having thoroughly characterized the response of individual particles to a homogenous dielectric medium, the focus can now be shifted to arrays. The additional layer of complexity in discussing arrays of plasmonic particles is due to the interference of the scattered radiation at the site of an individual particle. The

interference at a given center particle due to all of the other particles in the array can best be characterized in terms of the sum of the phase of all scattered light in the array, given by Eq. (7)<sup>25</sup>.

$$S_R = 4 \frac{C}{D} \sum_{i=1}^G \sum_{j=1}^G \frac{\sin^2(\theta)}{r} \cos(Ar) \quad (7)$$

where  $D$  is the lattice constant,  $C$  is the scattering amplitude,  $A=kD=2\pi\eta D/\lambda$  is the lattice parameter,  $r = \sqrt{i^2 + j^2}$  is the distance to a given particle,  $\theta = \tan^{-1}(j/i)$  is the angle from the horizontal to a particular particle, and  $G$  is the grid size related to the total number of particles,  $N$ , by  $N = (2G + 1)^2$  with the dielectric medium being accounted for in the lattice parameter. To analyze the effects of phase overlap in general,  $C/D$  was set to unity.

Shown in Figure 10 is a calculation of the phase overlap at the center particle (dotted lines) for a 201x201 array of 70 nm particles with 600 nm spacing for RIs of 1.00 (black), 1.17 (blue), and 1.33 (red). Immediately below  $\eta D$  for each RI value there is a negative value for the phase overlap indicating destructive interference. Values above  $\eta D$  are always positive but rapidly converge to zero in a damped, oscillatory fashion. Overlaid with the phase overlap are the corresponding extinction spectra for each RI value.

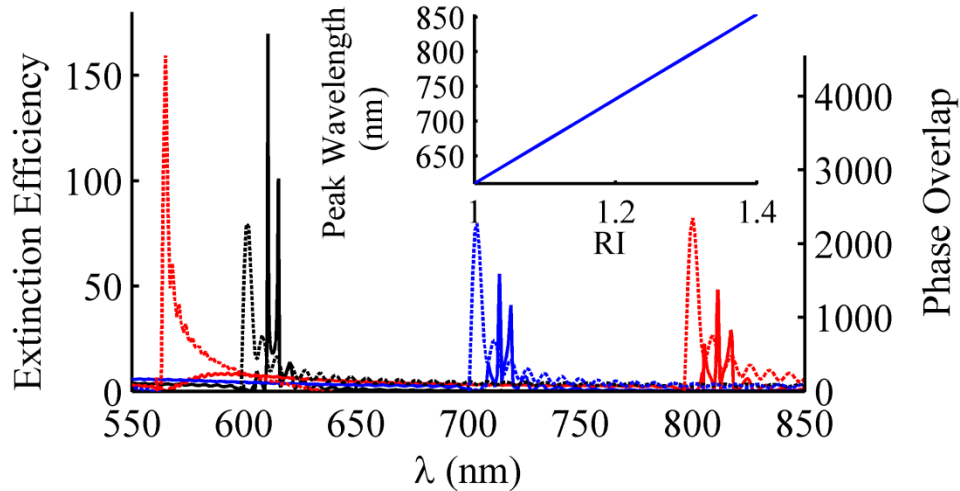


Figure 10. Reproduced from [13]. The dotted line represents the phase overlap on a center particle calculated by Eq. (6) for an array of 70 nm radius gold particles with a 600 nm spacing for RIs of 1.00 (black), 1.17 (blue), and 1.33 (red). Overlaid (solid lines) is the extinction spectra corresponding to the phase overlap plots. The inset shows the wavelength of the coupled peak maximum as a function of the RI.

The phase overlap calculated in Figure 10 displays two primary features for each RI corresponding to the overlap from axial and diagonal chains of particles (only for a RI of 1.33 (red curve) does the diagonal peak fall within the wavelength range displayed).

The remaining off-axial-off-diagonal (OAD) particle chains contribute by causing the oscillations in the phase overlap<sup>25</sup>.

In the inset of Figure 10, the wavelength corresponding to the coupled peak is displayed as a function of refractive index. As the RI increases, the peak redshifts linearly maintaining a nearly constant wavenumber. The slope of the inset line describes the sensitivity (peak shift per refractive index unit) of the coupled peak which is 608.2 nm/RIU for the array configuration in Figure 10.

A similar trend is observed in the dipole and quadrupole LSPR modes with shifting RI, but they exhibit much lower sensitivity. Using the array configuration presented in Figure 10, Figure 11 displays the extinction for wavelengths from 400-920 nm. The leftmost feature corresponds to the quadrupole mode of the LSPR while the middle feature corresponds to the dipole mode and the rightmost feature is the coupled peak. Each feature displays redshift with increasing RI, but the sensitivities are significantly different: 158.8 nm/RIU, 434.2 nm/RIU, and 603.8 nm/RIU for the quadrupole, dipole, and coupled peak respectively.

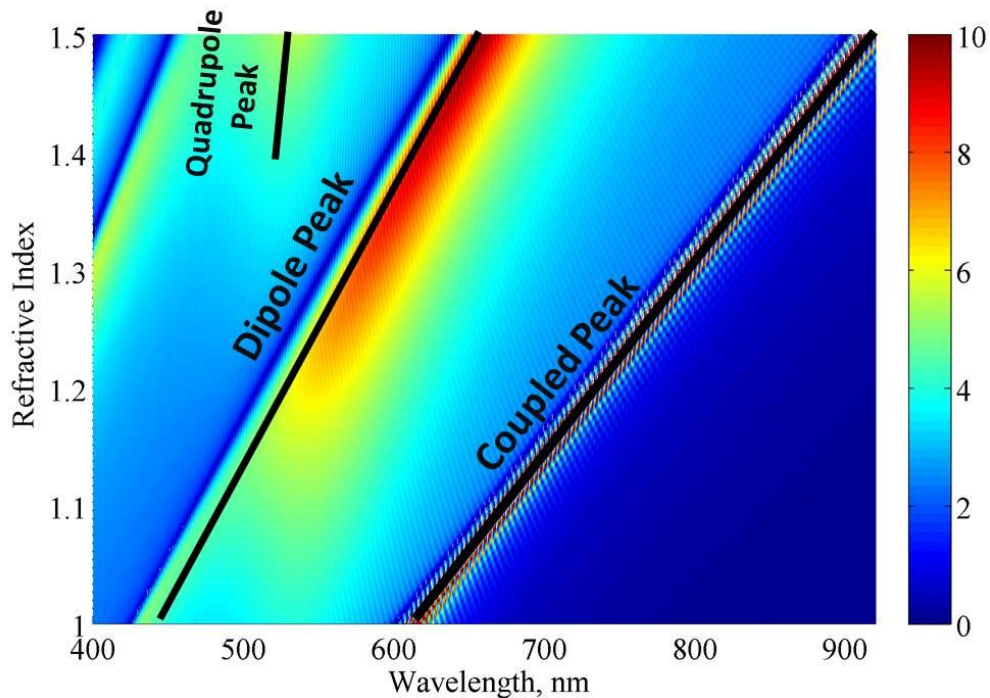


**Figure 11.** The extinction cross section (truncated at 10 in arbitrary units to display trends) is plotted for a 301x301 array of 70 nm, spherical, gold nanoparticles with a 600 nm lattice constant for wavelengths from 400 nm to 920 nm and refractive indices from 1 (vacuum) to 1.5.

When compared with Mie Theory these results can be used to show the dramatic increase in sensitivity that arrayed nanoparticles display relative to disordered arrangements of nanoparticles. Such arrangements would not exhibit the far-field

coupling associated with structured arrays meaning they would behave essentially as individual particles with regard to their sensitivity to changes in the medium RI. Such a response can be exactly modeled with Mie Theory to determine that a 70 nm gold particle would exhibit redshifts of 71 and 224 nm/RIU for the quadrupole and dipole modes respectively, values that are significantly lower than those for a structured array of the same particles.

### Geometry & Sensitivity

Due to the extra layer of complexity in the coupled peak's dependence on particle polarizability and lattice parameter, a single array geometry is not sufficient to characterize the effects of the local dielectric environment. Figure 12 presents the sensitivity of the coupled peak as a function of particle radius and lattice constant. The sensitivity was determined by subtracting the wavelength of the coupled peak at a RI of 1.0 from the wavelength at a RI of 1.1 and dividing by the difference in RI. A general trend is observed with increases in the sensitivity for larger particles and larger lattice constants with periodic linear deviations above and below the general trend. These deviations are attributed to geometric configurations that result in local constructive and destructive regions of scattered light.

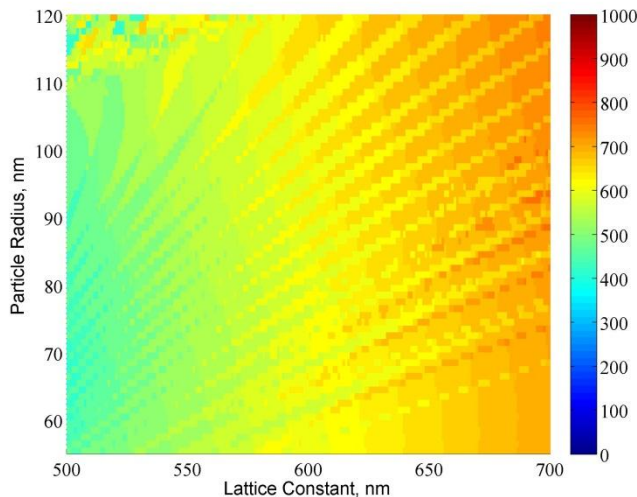


**Figure 12.** Sensitivity (nm/RIU) is plotted on the color scale as a function of the particle radius and lattice constant for a RI shift from 1.00 to 1.10. Specifically, the sensitivity is calculated from the difference in peak location for the two RI values divided by the change in RI, 0.10.

In addition to the sensitivity, the amplitude of the coupled peak is highly dependent on the geometric configuration of the array. Once again the patterns of constructive and destructive interference are the determining factor for the spectral properties. In Figure 13, Figure 6 is reproduced alongside a plot of an identical array for the same range of geometries but with a RI of 1.10. The observed trend is that there is a shift in the geometric configurations that allow constructive coupling to occur.

Specifically, with increasing RI the particle radii and lattice constants that allow constructive coupling to occur decrease.

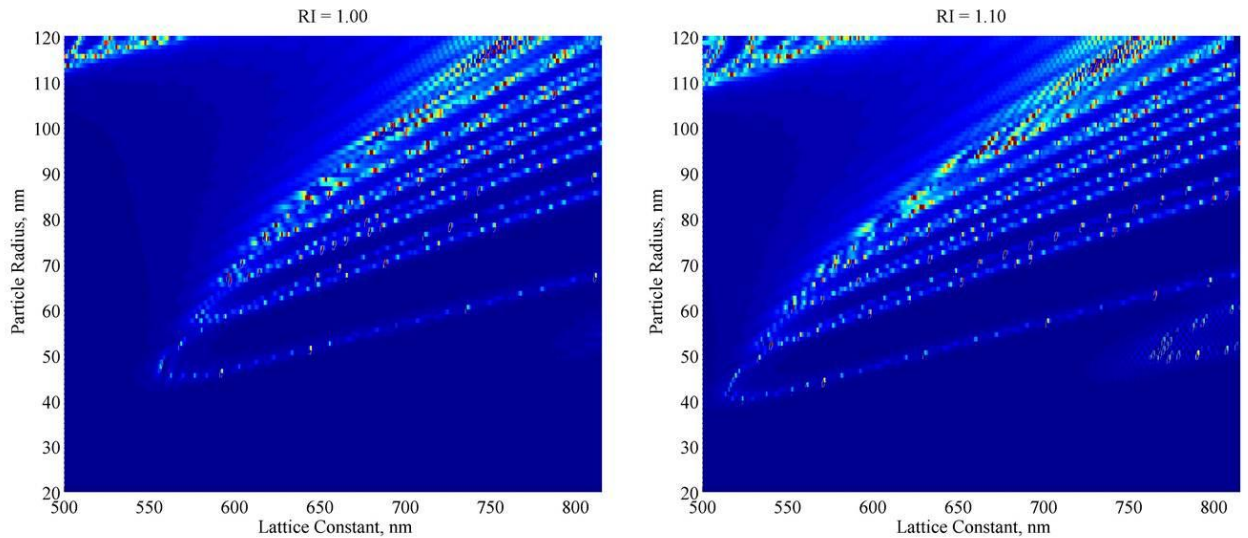


**Figure 13.** The amplitude of maximum extinction is plotted for a range of particle radii and lattice constants for two values of RI. Extinction values were truncated at 2000 to prevent the trends from being washed out by a few exceptionally tall peaks. The plot on the left is identical to Figure 6, and the plot on the right shows the results for the same array geometry but with a RI of 1.10.

The minimum lattice constant for coupling decreases because wavelength compression allows smaller lattice constants to support constructive interference as previously described and characterized by the lattice parameter,  $A$ . At first glance, this trend may appear to contradict the fact that coupling will not occur in vacuum for radiation with a wavelength shorter than the LSPR wavelength. For instance, at a RI of 1.33 and a particle radius of 40 nm the LSPR wavelength would be around 600 nm which can be seen in the polarizability plot of Figure 9. Meanwhile, the coupled peak for this configuration is maximized at a wavelength closer to 420 nm (data not shown)<sup>13</sup>, a significantly shorter wavelength than the LSPR wavelength. This issue is resolved by again considering the lattice parameter. The energy of the wave remains unchanged with changing RI; the RI simply reduces the minimum distance capable of supporting an integer number of wavelengths from particles along the axial chain.

Returning again to Figure 9 and the idea of polarizing the dielectric medium surrounding the array, the shift in particle radius can be explained. As previously described, increases in RI allow for more polarization of the dielectric medium which increases the amplitude of the particle polarizability. An additional trend that can be observed in Figure 13 is that the width of the lobes of constructive coupling decreases at higher RIs. This trend is the product of the relative change in particle radius and lattice constant that allows for constructive coupling at higher RIs. The scattered radiation is most strongly affected by the higher RI leading to a more rapid shifting in the lattice

constant that allows for coupling as compared to the shift in particle radius due to higher polarizabilities.

## **Conclusions**

In the end, the spectral properties of a square array of spherical, plasmonic nanoparticles have been fully described in terms of the polarizability of the individual particles and the relative phase of the scattered radiation in the plane of the array. By considering these two parameters, the complete parametric effects of the particle radius, spacing, and dielectric environment can be characterized within the limits discussed. The methods and principles presented here extend themselves quite naturally to non-spherical particle geometries and non-square nanoparticle arrangements assuming the dominant scattering mode would remain dipolar in nature. To model such systems, one would have to replace the chosen polarizability model with one suited to the desired geometry, which could vary dramatically in complexity depending on the dominant scattering modes, and adjust the retarded dipole sum to model the new particle arrangement. Different plasmonic materials than gold could also be considered by replacing the dielectric function of gold with that of the desired plasmonic material.

Using data obtained from simulations using the rsa-CDA model, the design specifications for a two-dimensionally arrayed, spherical, plasmonic material can be rapidly determined to suit a particular application. In roughly one hour the entire parameter space of particle radius and lattice constant can be mapped out in 1 nm increments for a particular background refractive index yielding the complete extinction profile for each geometry across the UV-vis spectrum with a wavelength resolution of 0.1 nm. Comparable results from other models for the investigated systems would likely take several days of computation time.

## REFERENCES

1. H. Lee, Y. Xiong, N. Fang, W. Srituravanich, S. Durant, M. Ambati, C. Sun, X. Zhang, "Realization of optical superlens imaging below the diffraction limit." *New J. Phys.* **7**, 255, (2005)
2. D. K. Gramotnev, S. I. Bozhevolnyi, "Plasmonics beyond the diffraction limit." *Nat. Photonics* **4**, 83-91, (2010)
3. J. Valentine, J. Li, T. Zentgraf, G. Bartal, X. Zhang, "An optical cloak made of dielectrics." *Nat. Mat.* **8**, 568-571, (2009)
4. X. Chen, Y. Luo, J. Zhang, K. Jiang, J. B. Pendry, S. Zhang, "Macroscopic invisibility cloaking of visible light." *Nat. Commun.* **2**, 176 (2011)
5. K. Kneipp, Y. Wang, H. Kneipp, L. T. Perelman, I. Itzkan, R. R. Dasari, M. S. Feld, "Single Molecule Detection Using Surface-Enhanced Raman Scattering (SERS)." *Phys. Rev. Lett.* **78**, 1667-1670, (1997)
6. A. Csaki, R. Möller, and W. Fritzsche, "Gold nanoparticles as novel label for DNA diagnostics," *Expert Rev. Mol. Diagn.* **2**, 187-193, (2002)
7. C. Gulmann, K. M. Sheehan, E. W. Kay, L. A. Liotta, and E. F. Petricoin III, "Array-based proteomics: mapping of protein circuitries for diagnostics, prognostics, and therapy guidance in cancer," *J. Pathol.* **208**, 595-606, (2006).
8. K. Hering, D. Cialla, K. Ackermann, T. Dörfer, R. Möller, H. Schneidewind, R. Mattheis, W. Fritzsche, P. Rösch, and J. Popp, "SERS: a versatile tool in chemical and biochemical diagnostics," *Anal. Bioanal. Chem.* **390**, 113-124, (2008).
9. F. J. Beck, S. Mokkaati, A. Polman, and K. R. Catchpole, "Asymmetry in photocurrent enhancement by plasmonic nanoparticle arrays located on the front or on the rear of solar cells," *Appl. Phys. Lett.* **96**, 033113 (2010).
10. S. Mokkaati, F. J. Beck, A. Polman, and K. R. Catchpole, "Designing periodic arrays of metal nanoparticles for light-trapping applications in solar cells," *Appl. Phys. Lett.* **95**, 053115 (2009).
11. J. Li, X. Hu, Y. Gu, and Q. Gong, "Tunable wavelength-division multiplexing based on metallic nanoparticle arrays," *Opt. Lett.*, **35**, 4051-4053 (2010).
12. D. K. Roper, P. Blake, D. DeJarnette, B. Harbin, "Plasmon coupling enhanced in nanostructured chem/bio sensors," In *Nano-plasmonics: Advanced Device Applications* J.W.M. Chon and K. Iniewski CRC Press (2012). In press.
13. D. DeJarnette, J. Norman, D. K. Roper, "Rapid attribution of Fano resonant band structures to particle size, lattice constant, and dielectric wavenumber in square nanoparticle arrays," In revision.
14. D. K. Roper, B. Taylor, B. Harbin, "Exact solutions to coupled dipole approximation of Maxwell's equations for periodic subwavelength nanostructures," Unpublished communication.

15. P. Blake, J. Obermann, B. Harbin, D. K. Roper. "Enhanced nanoparticle response from coupled dipole excitation for plasmon sensors," *IEEE Sensors* **11**, 3332-3340 (2011)
16. P. Blake, S. Kuhne, D. K. Roper, "Diffraction in ordered nanosphere arrays increases localized surface plasmon resonance sensitivity," In revision.
17. G. Mie, "Contributions on the optics of turbid media, particularly colloidal metal solutions." *Ann. Phys.* **25**, 377-345, (1908).
18. D. DeJarnette, D. K. Roper, B. Harbin, "Geometric effects on far-field coupling between multipoles of nanoparticles in square arrays." *J. Opt. Soc. Am. B* **29**, 88-99, (2012).
19. Y. Francescato, V. Giannini, and S. Maier, "Plasmonic systems unveiled by Fano resonances." *ACS Nano* **6**, 1830-1838 (2012).
20. W. T. Doyle, "Optical properties of a suspension of metal spheres." *Phys. Rev. B* **39**, 9852-9858, (1989)
21. L. Zhao, K. L. Kelly, G. C. Schatz, "The Extinction Spectra of Silver Nanoparticle Arrays: Influence of Array Structure on Plasmon Resonance Wavelength and Width," *J. Phys. Chem. B.* **107**, 7343-7350, (2003).
22. D. K. Roper, W. Ahn, B. Taylor, A. G. Dall'Asen, "Enhanced spectral sensing by electromagnetic coupling with localized surface plasmons on subwavelength structures." *IEEE Sens. J.* **10**, 531-540, (2010)
23. Y. Chu, E. Schonbrun, T. Ang, and K. B. Crozier, "Experimental observation of narrow surface resonances in gold nanoparticle array," *Appl. Phys. Lett.* **93**, 181108 (2008).
24. S. Zou and G. C. Schatz, "Narrow plasmonic/photonic extinction and scattering line shapes for one and two dimensional silver nanoparticle array," *J. Chem. Phys.* **121**, 12606-12612 (2004).
25. D. DeJarnette, J. Norman, and D. K. Roper, "Spectral patterns underlying polarization-enhanced diffractive interference are distinguishable by complex trigonometry." *Appl. Phys. Lett.* **101**, 183104 (2012).